ISPRS Journal of Photogrammetry and Remote Sensing 139 (2018) 103–118

Contents lists available at ScienceDirect

ISPRS Journal of Photogrammetry and Remote Sensing

journal homepage: www.elsevier.com/locate/isprsjprs

A new scheme for urban impervious surface classification from SAR images

Hongsheng Zhang [a,b], Hui Lin [a,b,c,*], Yunpeng Wang [d]

[a] Institute of Space and Earth Information Science, The Chinese University of Hong Kong, Shatin, New Territories, Hong Kong
[b] Shenzhen Research Institute, The Chinese University of Hong Kong, Shenzhen, China
[c] Department of Geography and Resource Management, The Chinese University of Hong Kong, Shatin, New Territories, Hong Kong
[d] Guangzhou Institute of Geochemistry, Chinese Academy of Sciences, Guangzhou, China

ARTICLE INFO

Article history:
Received 14 November 2017
Received in revised form 3 March 2018
Accepted 5 March 2018

Keywords:
SAR
Impervious surface
H/A/Alpha
VIS
Radsarsat-2

ABSTRACT

Urban impervious surfaces have been recognized as a significant indicator for various environmental and socio-economic studies. There is an increasingly urgent demand for timely and accurate monitoring of the impervious surfaces with satellite technology from local to global scales. In the past decades, optical remote sensing has been widely employed for this task with various techniques. However, there are still a range of challenges, e.g. handling cloud contamination on optical data. Therefore, the Synthetic Aperture Radar (SAR) was introduced for the challenging task because it is uniquely all-time- and all-weather-capable. Nevertheless, with an increasing number of SAR data applied, the methodology used for impervious surfaces classification remains unchanged from the methods used for optical datasets. This shortcoming has prevented the community from fully exploring the potential of using SAR data for impervious surfaces classification. We proposed a new scheme that is comparable to the well-known and fundamental Vegetation-Impervious surface-Soil (V-I-S) model for mapping urban impervious surfaces. Three scenes of fully polarimetric Radsarsat-2 data for the cities of Shenzhen, Hong Kong and Macau were employed to test and validate the proposed methodology. Experimental results indicated that the overall accuracy and Kappa coefficient were 96.00% and 0.8808 in Shenzhen, 93.87% and 0.8307 in Hong Kong and 97.48% and 0.9354 in Macau, indicating the applicability and great potential of the new scheme for impervious surfaces classification using polarimetric SAR data. Comparison with the traditional scheme indicated that this new scheme was able to improve the overall accuracy by up to 4.6% and Kappa coefficient by up to 0.18.

1. Introduction

1.1. Scientific significance of urban impervious surfaces

Among urban land covers, urban impervious surfaces mainly refer to the built-up areas, including pavements and rooftops, that can be made up of diverse materials, such as asphalt, concrete, plastic and metal materials. Conventionally, urban impervious surfaces have been identified as a critical indicator for the process of urbanization and for the environmental impacts of urbanization (Arnold and Gibbons, 1996; Weng, 2001; Wu and Murray, 2003; Zhang et al., 2015). They were commonly used in lots of studies on environmental consequences of urbanization (Arnold and Gibbons, 1996; Bannerman et al., 1993; Schueler, 1994; Sleavin et al., 2000), hydrological, atmospheric and environmental models to simulate and study the urban hydrological process (Arnold et al., 1982; Espey et al., 1966; Jacobson, 2011; Seabum, 1969; Yang et al., 2010), urban atmospheric process and urban climate change (Hu et al., 2014; Ooi et al., 2017), urban solar energy balance, urban land surface temperature and the urban heat island (Lu and Weng, 2006; Schueler, 1994; Slonecker et al., 2001; Weng et al., 2006; Yuan and Bauer, 2007), as well as socio-economic studies such as measurement of urban growth, estimation of population distribution, and variation of housing prices (Wu and Murray, 2003).

1.2. Urban land cover classification from synthetic aperture radar (SAR) data

Numerous studies have focused on the urban land use and land cover (LULC) mapping using various polarimetric SAR data. Since

* Corresponding author at: Institute of Space and Earth Information Science, The Chinese University of Hong Kong, Shatin, New Territories, Hong Kong.
E-mail addresses: zhangstream@gmail.com (H. Zhang), huilin@cuhk.edu.hk (H. Lin).

https://doi.org/10.1016/j.isprsjprs.2018.03.007
0924-2716/

the active and side-looking SAR is sensitive to the dielectric and geometric properties of urban land surface such as structure and surface roughness, SAR data provided complementary information for LULC (Calabresi, 1996; Henderson and Xia, 1997; Stasolla and Gamba, 2008; Zhang et al., 2012; Zhang et al., 2014). With a number of studies exploring SAR data using their backscattering and polarimetric information, the diversity and complexity of LULC were identified and reported (Dekker, 2003; Gamba and Aldrighi, 2012; Guo et al., 2014; Hu and Ban, 2012; Majd et al., 2012; Niu and Ban, 2013; Tison et al., 2004; Voisin et al., 2013; Zhang et al., 2012; Zhang et al., 2016; Zhang et al., 2014). For instance, different backscatters in the urban environment were analyzed to examined the single, double and triple bounce scattering mechanism in urban areas and concluded that dominant urban scatters are single bounce from roofs and double bounce from ground-wall structures (Dong et al., 1997). Various LULC classes were analyzed in urban areas using polarimetric SAR data (Gamba and Lisini, 2013; Li et al., 2010; Niu and Ban, 2013), with different polarimetric decompositions including Pauli, Freeman, Touzi, Cloud-Pottier and H/A/alpha decompositions (Bhattacharya and Touzi, 2011; Hariharan et al., 2016; Niu and Ban, 2013; Park and Moon, 2007; Pellizzeri, 2003). Different classification methods were employed to conduct the LULC classification such as the maximum likelihood based methods (Li et al., 2010; Wu et al., 2008), support vector machine (Zhang et al., 2010), adaptive Markov random field (Niu and Ban, 2014) and fuzzy classification (Park and Moon, 2007). Nevertheless, impervious surfaces were seldom focused in previous studies, with only a few studies using polarimetric SAR. Fully polarimetric Radarsat-2 data were combined with SPOT-5 data to extract impervious surfaces using C5.0 decision tree algorithm in Beijing, China (Guo et al., 2014). Dual polarimetric SAR data (e.g. ALOS/PALSAR) and single polarimetric SAR data (e.g. ENVISAT ASAR and TerraSAR-X) were also employed to extract impervious surfaces with the support of different optical satellite data (e.g. Landsat TM/ETM + and SPOT-5) in the metropolitan regions of the Pearl River Delta (Zhang et al., 2016; Zhang et al., 2015; Zhang et al., 2012; Zhang et al., 2014). Nevertheless, most of these studies followed the conventional scheme (i.e., vegetation, bright and dark impervious surfaces, bare soil and water surface), which does not consider the dielectric and geometric properties of urban land surface, which are the determining factors in SAR remote sensing data.

1.3. Previous scheme of impervious surfaces classification

Given its importance and wide applications, impervious surfaces classification (ISC) has been intensively studied using various types of space-borne and airborne remote sensing data. The first attempt can be dated back to the Vegetation-Impervious surface-Soil (VIS) conceptual model, where Ridd analyzed the composition of urban land covers and divided them into vegetation, impervious surface and bare soil, after masking out the water surface, which was considered to be relatively easily identified (Ridd, 1995). This study set up a theoretical model for ISC from remote sensing data. Following the VIS model, spectral mixture analysis (SMA) was employed to implement this conceptual model to estimate impervious surfaces at the sub-pixel level from satellite data. Wu and Murray (2003) applied this SMA method with the VIS model and further divided impervious surface into bright impervious surface and dark impervious surface after considering the significant differences in their spectral reflectance. This contribution provided the community with a better understanding of the composition of urban covers. A number of later studies have been conducted at the sub-pixel level, per-pixel level and segmented object level (Deng and Wu, 2013; Hu and Weng, 2009, 2011; Van de Voorde et al., 2011; Weng and Hu, 2008).

However, the composition of impervious surfaces in SAR data and their dielectric and geometric properties were insufficiently addressed in previous studies regarding the classification of urban impervious surfaces. This study aimed to develop a new scheme for impervious surfaces classification by investigating and understanding the composition of urban impervious surfaces in polarimetric SAR data. The compositions of land covers in the VIS model were re-examined under the context of their polarimetric mechanism in the SAR data, and thus various subclasses of each land cover class were identified to form the new scheme of ISC in polarimetric SAR data.

2. Study area and data sets

2.1. Study sites

The Pearl River Delta (PRD) has witnessed the most dramatic urbanization process in the world in the past four decades under the implementation of the *reform and opening* policy of the Chinese Government. Additionally, the PRD is a special metropolitan area because it includes three different urban planning and development policy bodies, Mainland China, Hong Kong and Macau. In PRD, numerous areas of urban impervious surfaces have been produced and have resulted in a wide range of environmental issues, such as urban flooding and air and water pollution. These impacts have been threatening the health of the environment and human beings in the whole PRD region, including Mainland China, Hong Kong and Macau. Continuous or timely monitoring of the urbanization dynamics using satellite remote sensing technology is important. However, the whole region is located in a subtropical climate zone, which is characterized by rainy and cloudy weather throughout the whole year. This weather brings great difficulties for optical remote sensing technology. Therefore, with the capability of penetrating clouds and rain, SAR remote sensing provides an ideal approach for monitoring the PRD area over a regional scale. In this study, three sites were carefully selected, including Shenzhen City from Mainland China, Hong Kong and Macau. The geographic locations of the study sites in the PRD are showed in Fig. 1. The Macau site actually includes a part of Zhuhai City (Wang Kam Island) from the Mainland.

2.2. Satellite data

Three scenes of fully polarimetric Radarsat-2 data at a fine resolution of 8 m were collected for the three study sites. The acquisition dates for the three Radarsat-2 data are listed in Table 1. These polarimetric SAR data were first calibrated using the Sentinel Application Platform (SNAP) toolbox provided by the European Space Agency (ESA). Various polarimetric decomposition methods were applied using SNAP. Detailed information about the decomposition methods were provided in Section 3.1. Finally, both the original SAR data and the polarimetric features were geocoded under the geo-reference systems of WGS 1984 and UTM projection system at Zone 49 N. Moreover, very high resolution optical satellite data from Worldview-2 and Google Earth at a spatial resolution of 2 m were used as the reference data. As shown in Table 1, the acquisition dates were very close to the acquisition dates of Radarsat-2 data in the three study sites. More details about the reference data are provided in Section 3.4.

3. Methodology

The methodology of this study is illustrated in the flowchart in Fig. 2, showing the proposed impervious surface classification scheme (within the dashed rectangle) and the working flow to

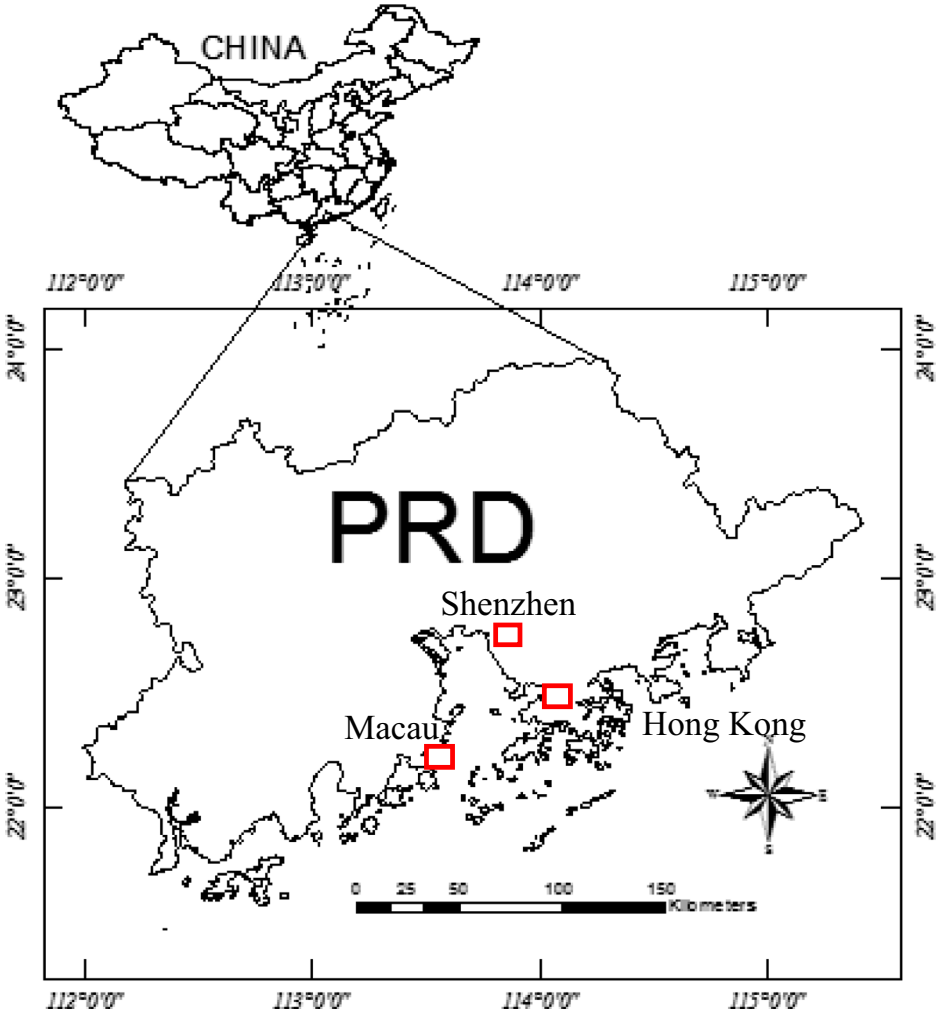

Fig. 1. Geographic locations of the study sites in the Pearl River Delta.

Table 1
The acquisition dates of the satellite data and field survey data used in this study.

Study site	Radarsat-2 data	Very high resolution reference data	Field survey data
Shenzhen	03 September 2014	29 October 2014	8 January 2016
Hong Kong	12 July 2015	16 January 2015	8 October 2013
Macau	03 September 2014	04 September 2014	13 April 2016

evaluate this proposed scheme. In general, the proposed scheme was based on the urban land cover scattering mechanism modeled by the H/A/Alpha decomposition. Nine subtypes of urban land covers can be identified according to their scattering mechanisms. Since different scattering mechanisms can also be reflected in various polarimetric features extracted from different decomposition methods, several typical decomposition methods were employed to evaluate the importance of different polarimetric features to the classification of the nine subtypes of land covers under the proposed classification scheme. Different parts of the methodological flowchart are described in details in this section.

3.1. Terrain scattering modeling and H/A/Alpha decomposition

In general, polarimetric SAR data include not only single, dual and fully polarimetric SAR data but also other data derived in other polarimetric modes (e.g., compact polarimetric data). To study the ISC in a more general sense, the fully polarimetric mode was employed in this study. The fully polarimetric SAR data can be described by the backscattering coefficient matrix ***S***:

$$S = \begin{pmatrix} S_{HH} & S_{HV} \\ S_{VH} & S_{VV} \end{pmatrix} \tag{1}$$

where S_{HH}, S_{HV}, S_{VH}, S_{VV} denote the backscattering coefficients on four different polarizations. In this study we accept the symmetric assumption between cross-polarized channels, and hence S_{HV} = S_{VH}. Then, the covariance matrix ***C*** and the coherency matrix ***T*** can be derived from the coefficient matrix and described as follows.

$$C = \begin{bmatrix} |S_{HH}|^2 & \sqrt{2}S_{HH}S_{HV}^* & S_{HH}S_{VV}^* \\ \sqrt{2}S_{HV}S_{HH}^* & 2|S_{HV}|^2 & \sqrt{2}S_{HV}S_{VV}^* \\ S_{VV}S_{HH}^* & \sqrt{2}S_{VV}S_{HV}^* & |S_{VV}|^2 \end{bmatrix} \tag{2}$$

$$T = \frac{1}{2}\begin{bmatrix} \left\langle |S_{HH}+S_{VV}|^2 \right\rangle & \langle (S_{HH}+S_{VV})(S_{HH}-S_{VV})^* \rangle & \langle 2(S_{HH}+S_{VV})S_{HV}^* \rangle \\ \langle (S_{HH}-S_{VV})(S_{HH}+S_{VV})^* \rangle & \left\langle |S_{HH}-S_{VV}|^2 \right\rangle & \langle 2(S_{HH}-S_{VV})S_{HV}^* \rangle \\ \langle 2S_{HV}(S_{HH}+S_{VV})^* \rangle & \langle 2S_{HV}(S_{HH}-S_{VV})^* \rangle & \left\langle 4|S_{HV}|^2 \right\rangle \end{bmatrix} \tag{3}$$

Then, polarimetric decomposition provides a good way to investigate the composition of various urban land covers with different geometric or dielectric information. A number of

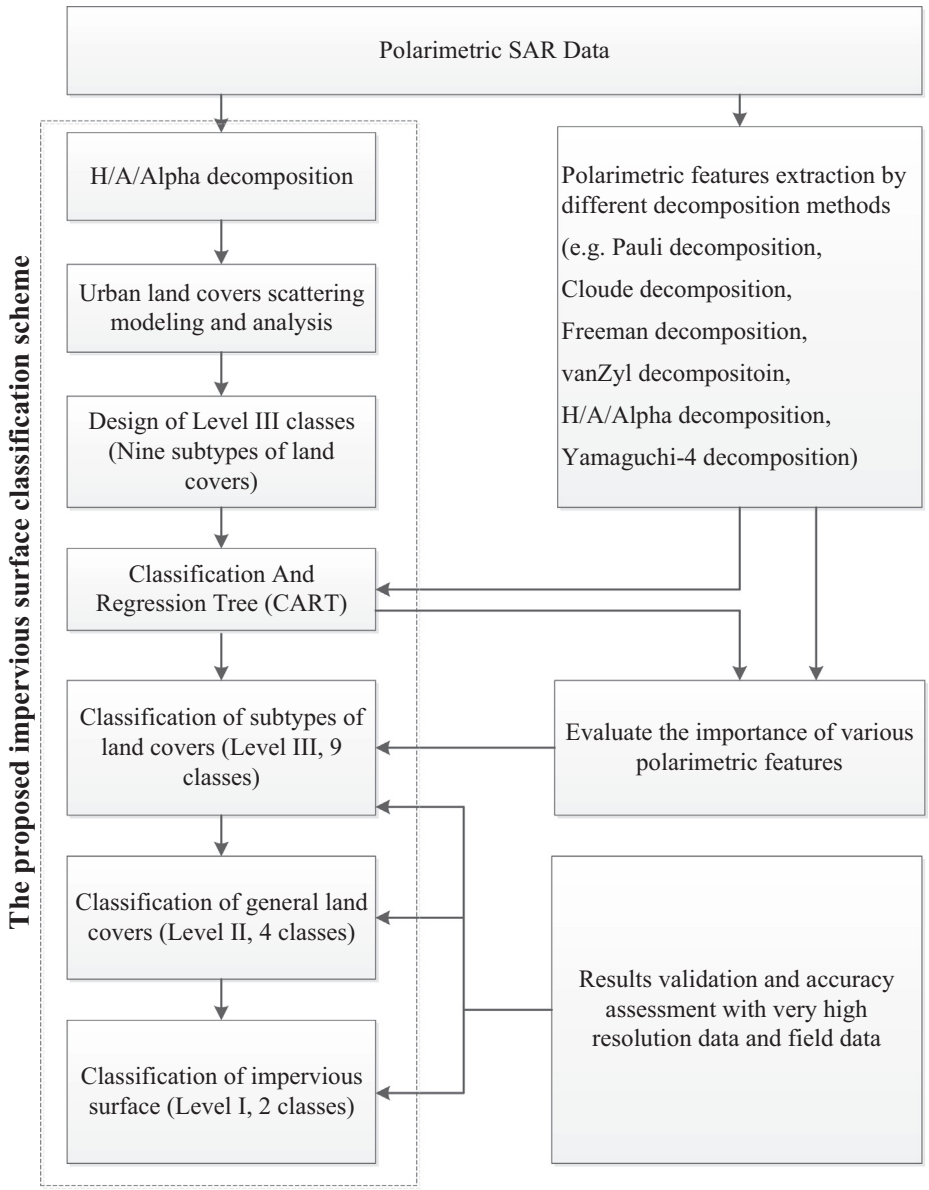

Fig. 2. Flowchart of this study and the proposed scheme.

polarimetric decomposition approaches have been proposed based on the decomposition of backscattering matrix ***S*** (e.g Pauli decomposition), covariance matrix ***C*** (e.g. Cloude decomposition, H/A/Alpha decomposition and Touzi decomposition) and coherency matrix ***T*** (e.g. Freeman decomposition, vanZyl decomposition and Yamaguchi decomposition).

The H/A/Alpha decomposition explains the mechanism of SAR imaging data, which is comparable to the VIS model in optical remote sensing data. In this decomposition, H is referred as the entropy and A is the anisotropy. Therefore, the H/A/Alpha decomposition was employed to investigate the composition of urban impervious surfaces to build a new scheme for ISC when using polarimetric SAR data. The following parts of this section give an introduction to the fundamental theory of this new scheme for ISC. By decomposing the coherency matrix, the eigenvalues and eigenvectors can be calculated. Next, the H/A/Alpha decomposition method can be applied with Eqs. (4)–(7).

$$P_i = \frac{\lambda_i}{\sum_{k=1}^{3}\lambda_k} \text{ with } \left(\sum_{k=1}^{3} P_k = 1\right) \tag{4}$$

$$H = \sum_{i=1}^{3} P_i log_2 P_i \tag{5}$$

$$A = \frac{\lambda_2 - \lambda_3}{\lambda_2 + \lambda_3} \tag{6}$$

$$Alpha = \sum_{i=1}^{3} P_i \alpha_i \tag{7}$$

where αi is the eigenvector parameter and λi ($\lambda 1 > \lambda 2 > \lambda 3$) are the eigenvalues in the coherency matrix ***T***. *Pi* is the pseudo probabilities, indicating the contribution of each λi. *H* is the scattering entropy. *A* is the scattering anisotropy describing the randomness of scattering. *Alpha* is related to the scattering direction. For instance, if the scattering occurs on a surface, *Alpha* value is 0. If it is the dihedral scattering, *Alpha* value is 90o. To understand the mechanism of different urban surfaces or targets, the *H*, *A* and *Alpha* can be split according to the split criteria in Table 2. The H-Alpha plane can be produced following the split criteria. In Table 2, there are mainly three ranges of *H*, referring to low entropy (0–0.5), medium entropy (0.5–0.9) and high entropy (0.9–1.0). For each entropy

Table 2
Split criteria of the H-Alpha plane.

H	[0 0.5]		[0.5 0.9]		[0.9 1.0]	
Alpha	7	[0 42.5]	4	[0 40]	1	[0 40]
	8	(42.5 47.5]	5	(40 50]	2	(40 55]
	9	(47.5 90]	6	(50 90]	3	(55 90]

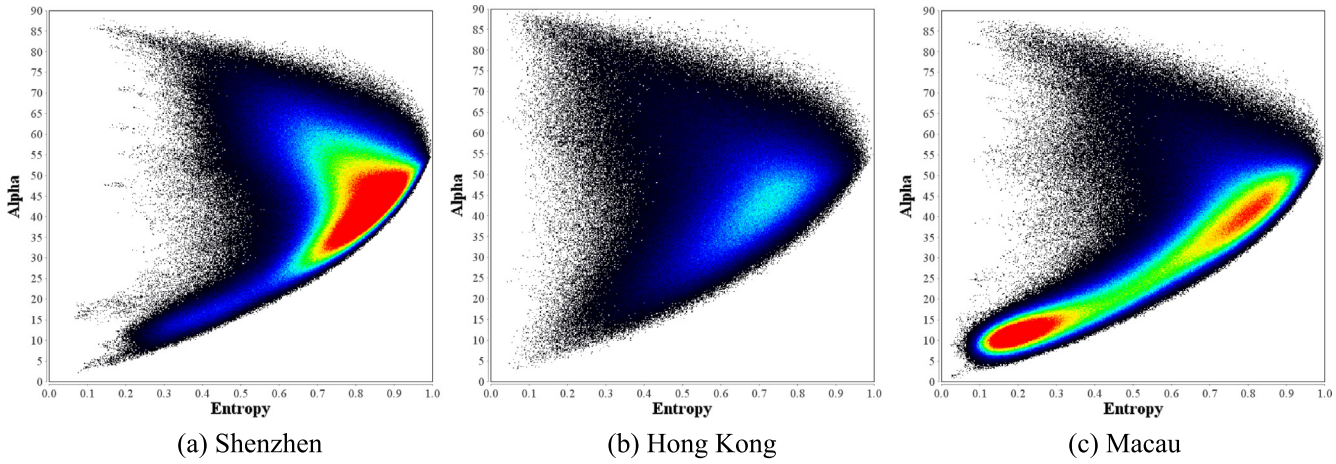

Fig. 3. The H-Alpha planes for the three study cases, warmer colors indicate denser points.

range, the *Alpha* is split into three ranges, which are different under different *H* ranges. The bounds values of this split criteria were firstly proposed by Cloude and Pottier (1997) based on the scattering mechanism analysis. So, they were chosen according to their physical characteristics but not mathematical inference. A detailed description of each scattering mechanism under this split criteria was provided in Cloude and Pottier (1997). This split of the H-Alpha plane was generically and thus did not depend on any polarimetric SAR data sets. Although there was no formal mathematical inference, they have been successfully applied in many researches with the same splitting criteria. Additionally, due to the averaging inherent in Eq. (7), not all the values of Alpha are available given a certain value of entropy (H), leading to a limited region in the H-Alpha plane. This limited region was described as feasible region and can be separated by two curves, the solid line in Fig. 4 (Cloude and Pottier, 1997). More details about the H/A/Alpha decomposition can be found in numerous previous publications (Cloude and Pottier, 1997; Lee and Pottier, 2009).

In this study, different polarimetric decomposition methods can explain the target scattering mechanisms in different ways or from different aspects. However, their basic scattering mechanisms mainly include three categories: surface scattering, volume diffusion scattering and double bounce scattering. The strategy of this study was to combine the components of different polarimetric decompositions together to provide a more comprehensive description of the real scattering processes of the targets. Fig. 3 demonstrates the H-Alpha planes for the three study cases. Different colors indicate the number of pixels with the corresponding Entropy and Alpha value, which reflect the dominant backscattering mechanism in that area.

Table 3 lists all of the polarimetric features extracted by the decomposition methods mentioned above. The elements of the coherency matrix are also included. For the convenience of explanation and discussion in the following sections of this paper, all the features are coded in Table 3.

3.2. The new scheme of impervious surfaces classification

The new scheme proposed in this study refers to the whole classification procedure of "9 classes (level III) to 4 classes (level II) to 2 classes (level I)", which is described in details in Fig. 4 and Table 4. The new scheme is different from the traditional scheme introduced in Section 1.3, where four land cover types (bright IS, dark IS, vegetation and soil) were only used. In the traditional scheme, bright IS and dark IS are defined according to the spectral reflectance of impervious surface. However, this definition becomes invalid in SAR images as radar is more sensitive to the geometric properties of land covers. Therefore, we propose a new scheme using nine land cover types at the beginning (level III) according to the backscattering features of land covers (Fig. 4). The new classification scheme starts from the H/A/Alpha decomposition to analyze various landscapes including urban landscapes and others. The theoretical distribution of these nine land covers type on the H-Alpha plane is shown in Fig. 4.

When considering urban landscapes, the nine different backscattering mechanisms can be specified according to various urban land covers and terrains. Conventionally, typical urban land cover types including vegetation, impervious surfaces, bare soil and water surface. In the conventional optical remote sensing data, water surface can be relatively easily identified due to its low reflectance. However, in the side-looking SAR data, water surface can have a relatively complex backscattering mechanism depending on its location and relationship to its surroundings (e.g., vegetation and buildings). Therefore, water surface may not be easily masked out when using polarimetric SAR data. Similarly, vegetation, impervious surfaces and bare soil can be complex depending mainly on their geometric structures, their alignments compared with the side-looking direction and their surface roughness compared with the wavelength of the microwave. With the analysis of the nine different mechanisms in the H-Alpha plane, the urban land covers were further divided into

Table 3
Polarimetric features used in this study.

Code	Name of features	Description	Code	Name of features	Description
B1	T11	B1-B9 are elements of the T matrix. T_{ij} is	B22	Lambda	B16-28 are components from
B2	T12_real	the *i*th row and *j*th column element	B23	Alpha1	H/A/Alpha decomposition
B3	T12_image		B24	Alpha2	
B4	T13_real		B25	Alpha3	
B5	T13_image		B26	Lambda1	
B6	T22		B27	Lambda2	
B7	T23_real		B28	Lambda3	
B8	T23_image		B29	Pauli_R	B 29-B31 are components from
B9	T33		B30	Pauli_G	Pauli decomposition
B10	Cloude_DBL	B10-B12 are components from Cloude	B31	Pauli_B	
B11	Cloude_VOL	decomposition	B32	Touzi_Psi	B31-B33 are components from
B12	Coude_SURF		B33	Touzi_A	Touzi decomposition
B13	Freeman_DBL	B13-B15 are components from Freeman	B34	Touzi_T	
B14	Freeman_VOL	decomposition	B35	Touzi_Phi	
B15	Freeman_SURF		B36	vanZyl_DBL	B36-B38 are components from
B16	Entropy	B16-28 are components from H/A/Alpha	B37	vanZyl_VOL	vanZyl decomposition
B17	Anisotropy	decomposition	B38	vanZyl_SURF	
B18	Alpha		B39	Yama_DBL	B39-B42 are components from
B19	Beta		B40	Yama_VOL	Yamaguchi decomposition
B20	Delta		B41	Yama_SURF	
B21	Gamma		B42	Yama_HLX	

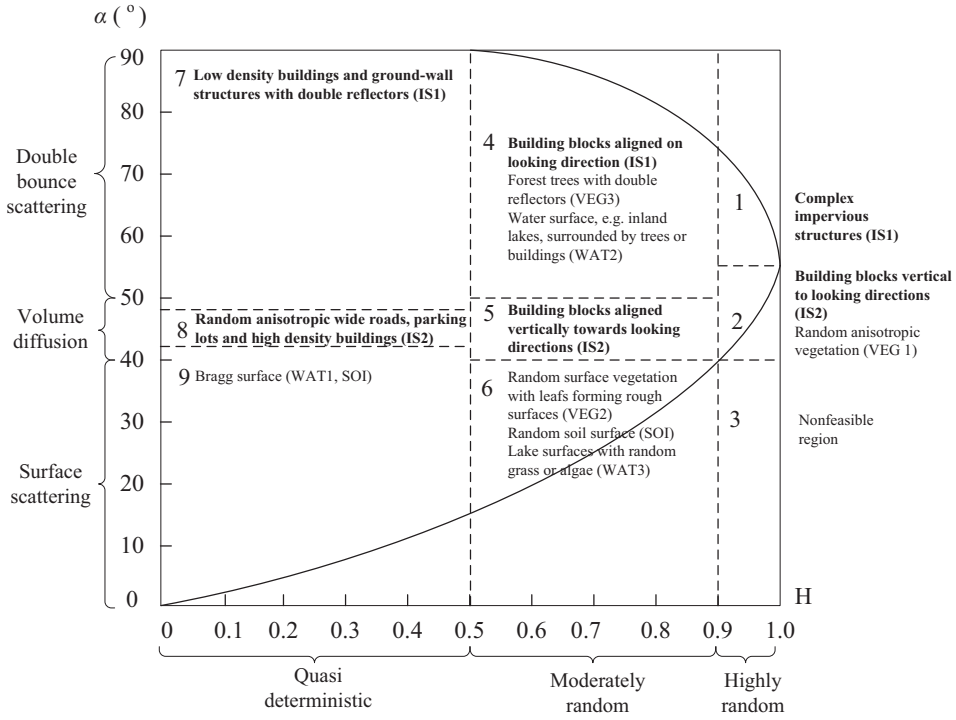

Fig. 4. Projection of urban impervious surfaces and other land covers on the H–α plane, the solid line separates the feasible region (left) and infeasible regions (right).

nine different types, include two types of impervious surfaces (IS1 and IS2), three vegetation types (VEG1, VEG2 and VEG3), three water types (WAT1, WAT2 and WAT3) and one type of bare soil (SOI).

Detailed definitions and descriptions of the nine types of urban land covers are provided in Table 4. For the two types of impervious surfaces, IS1 denotes the double reflection propagation impervious surfaces, which mainly include buildings aligned on the looking direction of the SAR satellites. Pavement, such as roads, highways and parking lots, aligned on the looking direction together with surrounding buildings, also falls into this category. Low density buildings and ground-wall structures with double reflectors also mainly fall into this category. IS1 falls within Zones 1, 4 and 7 on the H-Alpha plane, which are all characterized with double bounce scattering. IS2 denotes the random anisotropic impervious surfaces, which mainly include buildings and pavement aligned not parallel to the radar flight pass. IS2 also includes wide roads, parking lots and high density and small buildings with irregular alignment. IS2 falls mainly within Zones 2, 5 and 8 on the H-Alpha plane, which are characterized with volume scattering. Vegetation was divided into three sub-categories: random anisotropic vegetation (VEG1), random surface vegetation (VEG2) and double reflection propagation vegetation (VEG3). Vegetation is one of the most complex terrains for SAR remote sensing data. Vegetation can have diverse scattering mechanisms corresponding to the structures of leafs, tree types, stands, growing stages, and

Table 4
New definitions of urban land covers with polarimetric SAR data.

Land Cover Types (Level I)	Land cover Subtypes (Level II)	Subtypes under the new scheme (Level III)	Basic description
Impervious Surfaces (IS)	IS	IS1	Double reflection propagation impervious surfaces: medium entropy, building blocks and pavement aligned on looking directions, low density buildings and ground-wall structures with double reflectors. IS1 is located mainly in Zones 1, 4 & 7
		IS2	Random anisotropic impervious surfaces: high entropy, building blocks and pavement aligned vertically to looking directions, wide roads, parking lots and high density buildings. IS2 is located mainly in Zones 2, 5 & 8
Non-Impervious Surfaces (NIS)	Vegetation (VEG)	VEG1	Random anisotropic vegetation, high entropy vegetation scattering (needles types), almost no polarization dependence. It is mainly located in Zone 2
		VEG2	Random surface vegetation, medium entropy, vegetation with surface roughness (leafs). It is mainly located in Zone 6
		VEG3	Double reflection propagation vegetation, medium entropy multiple scattering, double reflection occurs with propagation through a canopy. It is mainly located in Zone 4
	Water (WAT)	WAT1	Brag water surface, very smooth water surface, low entropy, and coastal sea water. It is mainly located in Zone 9
		WAT2	Double reflection water surface, inland lakes surrounded by trees or buildings. It is mainly located in Zone 4
		WAT3	Random surface water, medium entropy water surface, inland lakes with random plants (random roughness). It is mainly located in Zone 6
	Bare soil (SOI)	SOI	Random surface bare soil, medium entropy with random surface roughness. It mainly falls into Zones 6 and 9

forest types. The three types of vegetation fall within Zones 2, 6 and 4, respectively. Water surfaces were also divided into three sub-categories, the Brag water surface (WAT1), double reflection water surface (WAT2) and random water surface (WAT3). Commonly, open waters with large surface areas and without surrounding buildings or vegetation should be characterized by Brag scattering. However, if the water body (e.g., lakes and rivers) are surrounded by buildings or trees, it can appear as double or random scattering. Moreover, algae or algal blooms in the lakes can increase the roughness of water surface, making it a random water surface. It should be noted that WAT2 and WAT3 may not always be present in any areas, depending on the specific landscape. The three types of water surfaces mainly fall within Zones 9, 4 and 6, respectively. Lastly, the bare soil is often characterized by random scattering and falls within Zones 6 and 9. Compared to the case in optical data where bare soils are often confused with bright or dark impervious surfaces, the bare soil in polarimetric SAR data is relatively simple to identify from impervious surfaces.

From the description and discussion of the impervious surfaces and non-impervious surfaces, three important comments should be noted. First, ISC from polarimetric SAR data is a totally different task compared with ISC from optical data. For instance, the common bright impervious surfaces and dark impervious surfaces in optical data have a totally different meaning in polarimetric SAR data. In optical data, high or low spectral reflectance depends on the material or chemical composition of the land surface. However, in SAR data, high or low backscattering coefficients depends on the geometrically properties of the surfaces, with little impacts from the materials. Therefore, the approaches to extract bright and dark impervious surfaces from optical data cannot be applied to SAR data for the same purpose. Instead, in this study, double reflection propagation impervious surfaces (IS1) and random anisotropic impervious surfaces (IS2) are identified from polarimetric SAR data. The vegetation, water and bare soil are also different than those derived from optical data. Secondly, ISC from polarimetric SAR data is not an easy task due to the diversity and confusion of scattering mechanisms between impervious surface types and non-impervious surface types. For instance, the land cover types of IS1, VEG3 and WAT2 all fall within Zone 4 and share similar scattering characteristics in polarimetric SAR data. Furthermore, it is difficult to extract one impervious surface type accurately since it falls into different zones. For instance, IS1 falls into Zones 1, 4 and 7, and in each zone, there are different confusions and mixtures between IS1 and other non-impervious surface types. Thirdly, vegetation is the most challenging land cover to separate from impervious surfaces. There are several confusions between these two major land cover types, including the confusion between IS2 and VEG1 in Zone 2, confusion between IS1 and VEG3 in Zone 4, and potential confusion between IS2 and VEG 2 in Zones 5 and 6. Generally, the success of ISC in polarimetric SAR data under the new scheme would mainly depend on the solution to these three issues.

3.3. ISC with classification and regression tree (CART)

CART was selected as the classification method based on the polarimetric features. CART is one of the best classifiers according to the literature. It is a good classifier that is comparable to other frequently used ones, such as support vector machine and random forest. The most important reason we chose CART was that it provides an understandable and comprehensive decision tree, which show how different land cover classes are identified in the decision tree.

Conventionally, several algorithms have been proposed to build a CART based on the training samples in a supervised manner, including the Fast Algorithm for Classification Trees (FACT), Classification Rule with Unbiased Interaction Selection and Estimation (CRUISE), Generalized, Unbiased Interaction Detection and Estimation (GUIDE) and Quick, Unbiased, Efficient, Statistical Tree (QUEST) (Loh, 2011). The measurement criteria of node impurity and node splits are slightly different using different algorithms, while the applications of the built-up CART for different algorithms are exactly the same. In this study, the CRUISE was employed to build the CART for urban land cover classification. CRUISE uses unbiased multiway splits, which were reported to have negligible bias in variable selection (Kim and Loh, 2001). A detailed description of the principles of the CRUISE algorithm is found in Kim and Loh (2001).

Three CARTs were built based on the training samples to classify the Radarsat-2 data of the three study cases. The CART was composed of decision nodes and result nodes. Decision nodes were built to decide which branch should go on the decision tree based on the judging condition of each decision node. Each judging condition was for one feature band in Table 3 and was generated by

the CRUISE algorithm. Result nodes were the leaves of the decision tree and represented the final decision of land cover types from all previous parent decision nodes. Finally, a total of 147 nodes were built for the Shenzhen case, 59 nodes for the Hong Kong case and 145 nodes for the Macau case.

3.4. Validation and accuracy assessment

3.4.1. Reference data for validation

Reference data of various urban land cover classes in the three selected sites under the new classification scheme were obtained by a field survey and visual interpretation of corresponding very high resolution optical satellite images. Generally, reference samples were collected randomly following the simple random schema and cluster schema (Jensen, 2007; Zhang et al., 2013). This combined random sampling schema considered both the correlations among neighbor pixels and the labor work during sampling in the field survey and visual interpretation over high resolution images. In this study, three field surveys were conducted in the PRD region from 2013 to 2016, including one survey in Yuen Long, Hong Kong in October 2013, one survey in Shenzhen, Mainland China in January 2016 and one survey in Taipa, Macau in April 2016. Location information and on-site photos for various land cover types were taken during the field survey in the study sites. However, the dates of these field surveys were not strictly the same as the dates of the satellite data used in this study. To avoid any possible land cover changes, very high resolution optical satellite data from Worldview-2 and Google Earth were used for selecting the reference data by visual interpretation with the aid of the collected field data. Finally, a set of reference samples were carefully selected for the three study sites, which are listed in Table 5. A total of 2910 samples (pixels) were selected in Shenzhen, 3068 samples in Hong Kong and 2702 samples in Macau. The class WAT2 was not present in the Macau site because there were no inland lakes surrounded by tall trees or tall buildings. These samples were selected according to the new classification scheme under the new subtypes of land covers defined in Table 5. For each site, 40% of the samples were selected for training the classifier, while 60% were selected for testing the accuracy of the results. This portion was determined empirically with a consideration of testing the robustness of the methodology. Previously, we used a portion of 30–60% to set the training samples out of all the samples, and a portion of 40–70% to set the testing samples (Zhang et al., 2018; Zhang et al., 2016; Zhang and Xu, 2018; Zhang et al., 2014). To select the portion of training and testing samples, it is assumed that a lower portion of training samples can better reflect the effectiveness of the proposed methodology (Zhang et al., 2018).

3.4.2. Accuracy assessment

The results of the classified urban land covers and estimated impervious surfaces were validated with the testing samples described in Table 5. The assessment included three different aspects. First, in the built CART models, the number of decision nodes can be used to indicate the importance of every polarimetric feature derived from various decomposition methods, while the number of result nodes (leaves) can represent the complexity of the land cover classes or subclasses. Therefore, these two indices were employed to assess and analyze the importance of extracted features and the complexity or difficulty of each land cover type. Secondly, the conventional confusion matrix was employed to compute the overall accuracy, Kappa coefficient, producer's accuracy and user's accuracy based on the testing samples. Details on how to calculate and understand the confusion matrix and related accuracy measures can be found in numerous publications (Jensen, 2007; Zhang et al., 2013). Thirdly, the evaluation of the number of nodes in CARTs and the confusion-matrix-based accuracies were applied at three different levels: the land cover subtypes level (Level III), reflecting the backscattering mechanism of each type; the general land cover level (Level II), representing the conventional land covers; and the impervious surfaces classification (Level I), indicating the final results of estimated impervious surfaces.

Table 5
Distribution of reference samples at the three sites (40% for training and 60% for testing).

Subtypes under the new scheme	Shenzhen	Hong Kong	Macau
IS1	317	316	403
IS2	321	430	316
VEG1	303	406	315
VEG2	437	328	321
VEG3	312	306	309
WAT1	237	313	342
WAT2	315	308	–
WAT3	299	347	345
SOI	369	314	351
Total samples	2910	3068	2702

4. Results and discussion

4.1. Polarimetric decomposition using different models

Polarimetric features were obtained by applying various decomposition methods. These polarimetric features reflect the backscattering mechanisms between the microwave and the land surfaces. Figs. 5–7 demonstrate the false color composition of the polarimetric features under different decompositions in the three study cases. In these figures, different colors represent different backscattering types. From these figures, land covers such as vegetation, water surface and urban areas can be generally separated. However, a complex scene can be observed in the urban areas, where several different colors were highly mixed together, indicating the complex backscattering mechanisms in urban areas. In general, the colors are consistent between Pauli decomposition and vanZyl decomposition, as well as between Freeman and Yamaguchi Four-Component Decomposition (Yamaguchi-4). The color representations of Cloude decomposition and the H/A/Alpha decomposition are different from others.

The false color composition in Hong Kong was generally consistent with the one in Shenzhen. The Cloude decomposition had similar colors as the Pauli and vanZyl decompositions. The urban area was characterized by various and fragmented land covers with different colors. There are many small boats on the northwestern corner of the image that were mistakenly identified as vegetation.

The false color polarimetric feature compositions in Macau are shown in Fig. 7. The patterns were generally consistent with that from the Shenzhen case. Compared with the previous two study sites, the surrounding areas in this image were mainly sea surface, which can be relatively easy to identify in all types of polarimetric decomposition results. Moreover, there was proportionally less urban area in Macau, and it was mixed with different land cover types.

4.2. Land cover classification results at different levels

The urban land covers were classified using the polarimetric features under the new classification scheme, which is shown in Fig. 8(a)–(c). Various impervious surfaces types were mixed together in the urban area, while various vegetation types were highly mixed in the mountain and urban areas. Water surfaces could generally be classified, but there were still mixtures in the

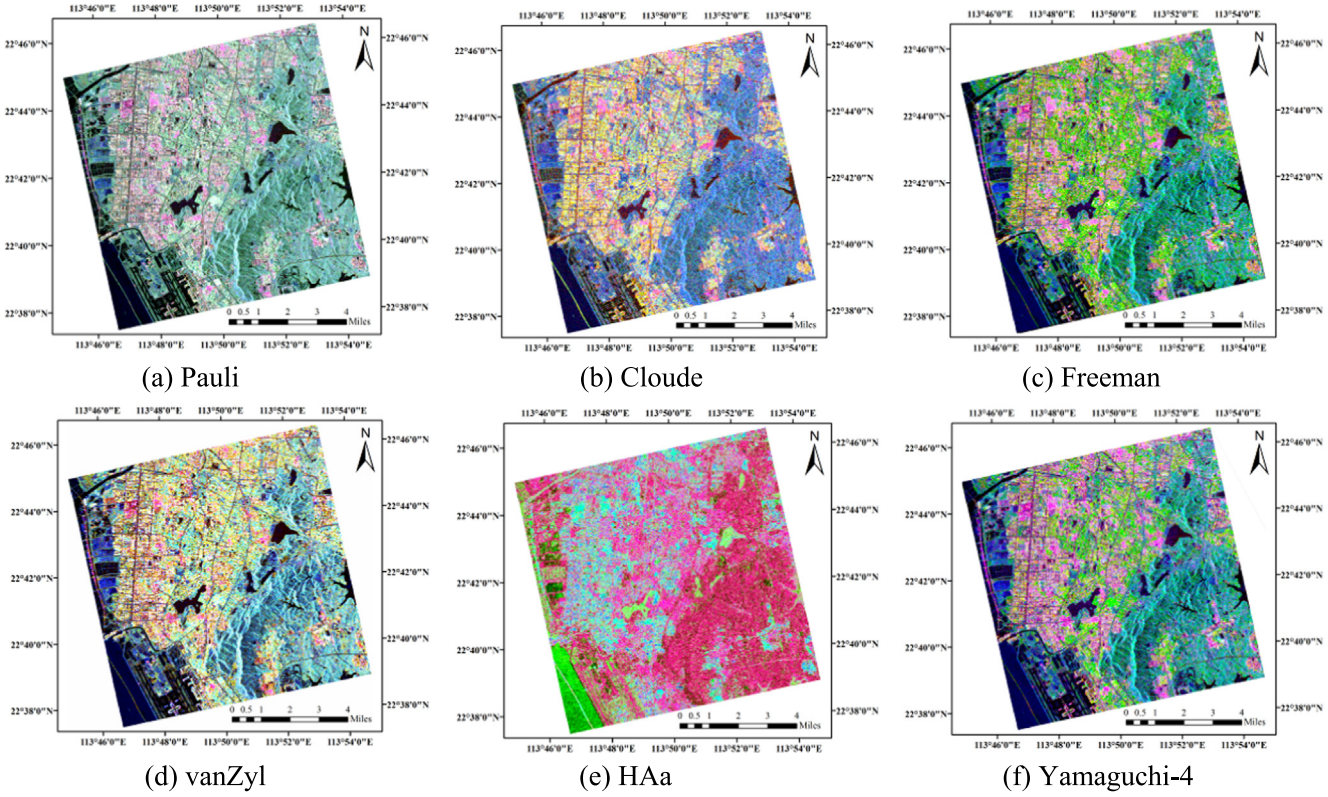

Fig. 5. Typical polarimetric decompositions (Shenzhen), referring to the name of features in Table 3, the R-G-B false color in each sub-figure is composited as (a) Pauli_R : Pauli_G : Pauli_B, (b) Cloude_DBL : Cloude_VOL : Cloude_SURF, (c) Freeman_DBL : Freeman_VOL : Freeman_SURF, (d) vanZyl_DBL : vanZyl_VOL : vanZyl _SURF, (e) Entropy : Anisotropy : Alpha, (f) Yama_DBL : Yama _VOL : Yama _SURF. (For interpretation of the references to colour in this figure legend, the reader is referred to the web version of this article.)

open sea water, particularly in the northwestern part of Hong Kong.

The new classification scheme is proposed based on the backscattering mechanisms, and these land cover subtypes do not have physical meanings for urban land cover management. Therefore, these land cover subtypes at Level III were combined to the land covers at Level II, which are the traditional land covers. Fig. 8(d)–(f) demonstrates the results of land cover classification at Level II, including the water surfaces, vegetation, impervious surfaces and bare soil. In the Level II classification results, small boats in all the three study cases were clearly identified, which is quite different from the traditional case in optical remote sensing applications. Theoretically, small boats cannot be clearly identified from satellite data at a resolution of approximately 8 m. Boats are often made of metal materials, which are electrically conducted and can strongly reflect the microwave from SAR satellites. This makes the backscattering signals stronger than usual land surfaces and results in a clear presence in the SAR data. From Fig. 8(d)–(f), these boats were recognized as both vegetation and impervious surfaces because they contribute to double bounce reflectance, which can be found in both impervious surfaces (e.g., tall buildings) and vegetation (e.g., tall trees).

Finally, the land covers at Level II were combined to the impervious surfaces at Level I, which is demonstrated in Fig. 8(g)–(i). Three different patterns of the distribution of impervious surfaces can be observed in Fig. 8(g)–(i), showing a highly urbanized area in Shenzhen, a median urbanized or suburban area in Hong Kong, and a small urbanized region in Macau. The small urbanized region is Wang Kam Island, which is mainly rural area and mountain and belongs to Zhuhai, an adjacent city next to Macau. However, there was noise of impervious surfaces in the vegetation area in all the three study cases, indicating the complex confusion between impervious surfaces and vegetation in polarimetric SAR data. The confusion can be interpreted from the definition of the new classification scheme in Fig. 4 and Table 4. A more insightful discussion will be provided in Section 4.4.

4.3. Importance of various polarimetric features

The number of decision nodes for a polarimetric feature in the CART can indicate the importance of that feature. Therefore, statistics were calculated through the whole CART model for all the polarimetric features. Interestingly, not all the features were actually used in the CART to conduct the land cover classification, but some features were used many times. Fig. 9(a, c & e) show the statistical results for the three study sites. In Shenzhen, the Entropy from the H/A/Alpha decomposition was used 21 times in the whole decision tree. The Freeman_VOL component from Freeman decomposition and the Alpha from H/A/Alpha decomposition were used 8 times. Other components from H/A/Alpha decomposition included Alpha1, Anisotropic and Lambda features, which were used 6, 3 and 3 times, respectively. In addition, the Touzi_Psi component from Touzi decomposition was also used 5 times. As a result, the H/A/Alpha decomposition was the most important decomposition for land cover classification under the new definition of land covers. In Hong Kong, the H/A/Alpha components Alpha, Lambda2, Anisotropy and Alpha1 were used 7, 5, 3 and 2 times in the decision tree, respectively, indicating the importance of this decomposition. However, the vanZyl decomposition (vanZyl_VOL) was also important and had 7 decision nodes in the CART. Other important decompositions included the element of T matrix (T22) and the Cloude decomposition (Cloud_DBL). In Macau, the H/A/Alpha

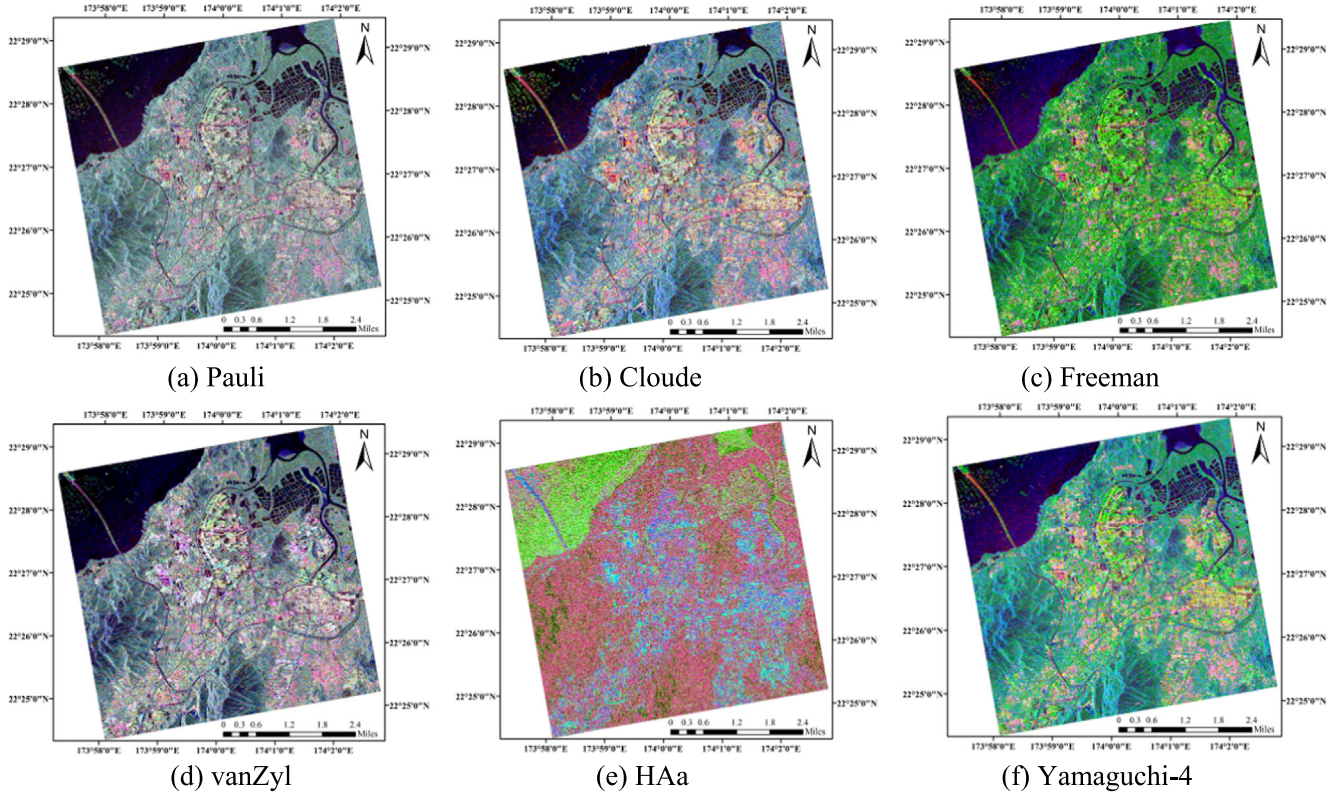

Fig. 6. Typical polarimetric decompositions (Hong Kong), referring to the name of features in Table 3, the R-G-B false color in each sub-figure is composited as (a) Pauli_R : Pauli_G : Pauli_B, (b) Cloude_DBL : Cloude_VOL : Cloude_SURF, (c) Freeman_DBL : Freeman_VOL : Freeman_SURF, (d) vanZyl_DBL : vanZyl_VOL : vanZyl _SURF, (e) Entropy : Anisotropy : Alpha, (f) Yama_DBL : Yama _VOL : Yama _SURF. (For interpretation of the references to colour in this figure legend, the reader is referred to the web version of this article.)

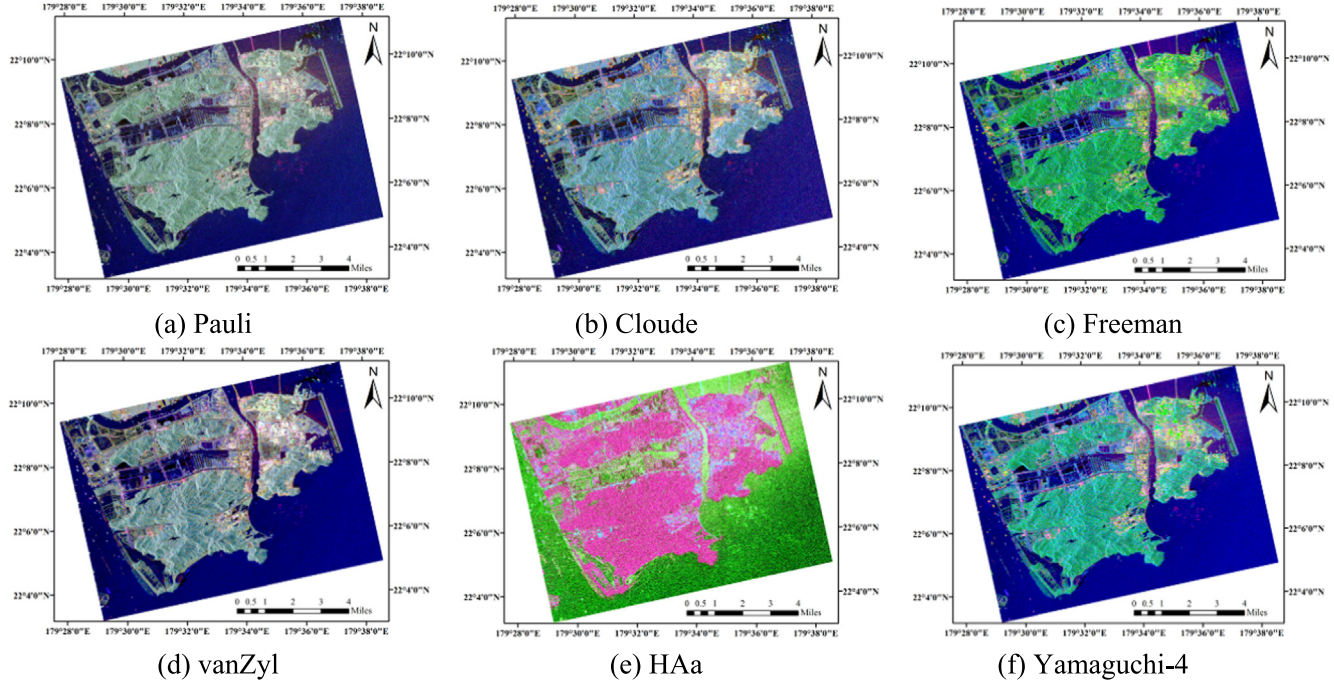

Fig. 7. Typical polarimetric decompositions (Macau), referring to the name of features in Table 3, the R-G-B false color in each sub-figure is composited as (a) Pauli_R : Pauli_G : Pauli_B, (b) Cloude_DBL : Cloude_VOL : Cloude_SURF, (c) Freeman_DBL : Freeman_VOL : Freeman_SURF, (d) vanZyl_DBL : vanZyl_VOL : vanZyl _SURF, (e) Entropy : Anisotropy : Alpha, (f) Yama_DBL : Yama _VOL : Yama _SURF. (For interpretation of the references to colour in this figure legend, the reader is referred to the web version of this article.)

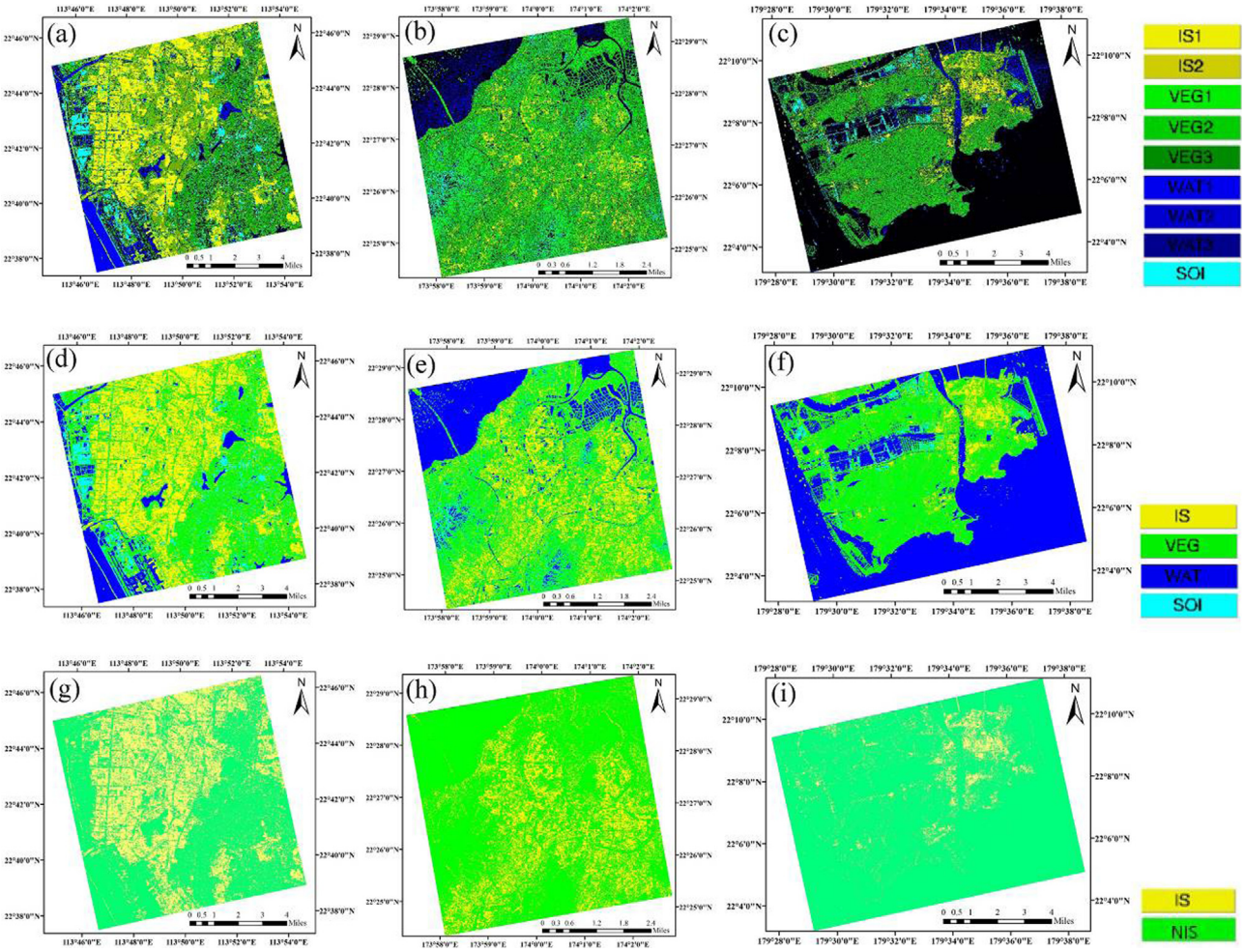

Fig. 8. LULC classification at different levels, (a)–(c) original classes, (d)–(f) subclasses combined, (g)–(i) combined impervious surfaces and non-impervious surfaces.

decomposition was a dominant contributor to the classification, with the components of Alpha, Anisotropy, Entropy, Lambda4 used 16, 11, 10 and 4 times, respectively, among a total of 72 decision nodes in the CART. Therefore, 57% of the decision nodes were based on the H/A/Alpha decomposition. Other important components included the vanZyl decomposition (vanZyl-DBL) and Yamaguchi 4-component decomposition (Yama_VOL).

Additionally, another aspect to reflect the importance of feature in CART is the impurity of each node. During the training of CART, Gini index was used as a measure of impurity to evaluate the importance of variables (features) to optimize each node. Gini index was within the range between 0 and 1. Commonly, a lower impurity (Gini index) value indicates a better split in a node based on the separation of the samples being considered. Therefore, the impurity measure of a feature in a node can reflect the importance of that feature on the node, but cannot reflect its importance on the whole decision tree as the impurity does not consider the frequency of the feature used in the whole decision tree. In this study, as additional information to assess the importance of features, the average Gini index of each feature was calculated over the whole CART by averaging the Gini index values in all the nodes that used the corresponding feature. Fig. 9(b, d & f) demonstrate the statistics of the average Gini index of those features with lower values in all the three study cases. Generally, the most pure features in the CART were not those most frequently used features. From the results, the elements in the ***T*** matrix tended to be more pure than other features from polarimetric decompositions, especially the case in Shenzhen (Fig. 9d). The results were reasonable since the local importance and global importance of a feature were not necessarily consistent when building the CART. For instance, one feature with low impurity indicates it is important to split the node with a given subset of samples. Thus, this importance is only applicable over the subset of samples. If the feature is not used frequently in the whole CART, it means it is not so important in other samples. That is to say, the Gini index reflects the local importance of features.

Therefore, the importance analysis of these decision nodes in the three cases indicated that the H/A/Alpha is the most important polarmetric decomposition for the land cover classification under the new scheme, while the other features provided important supplementary information at the local scale during the classification procedure. This result supports the fundamental theory of the proposed methodology to identify the distribution of various backscattering mechanisms and the distribution of various land covers on the H-Alpha plane. Additionally, other decompositions can also provide some complementary information, such as the Freeman decomposition, vanZyl decomposition, Cloude decomposition, Touzi decomposition and Yamaguchi decomposition. Especially, from the evaluation of node impurity, the elements of T matrix illustrated local importance in determining some nodes in the CART model. However, their contributions varied in different cases, and one part of their components contributed to the CART models.

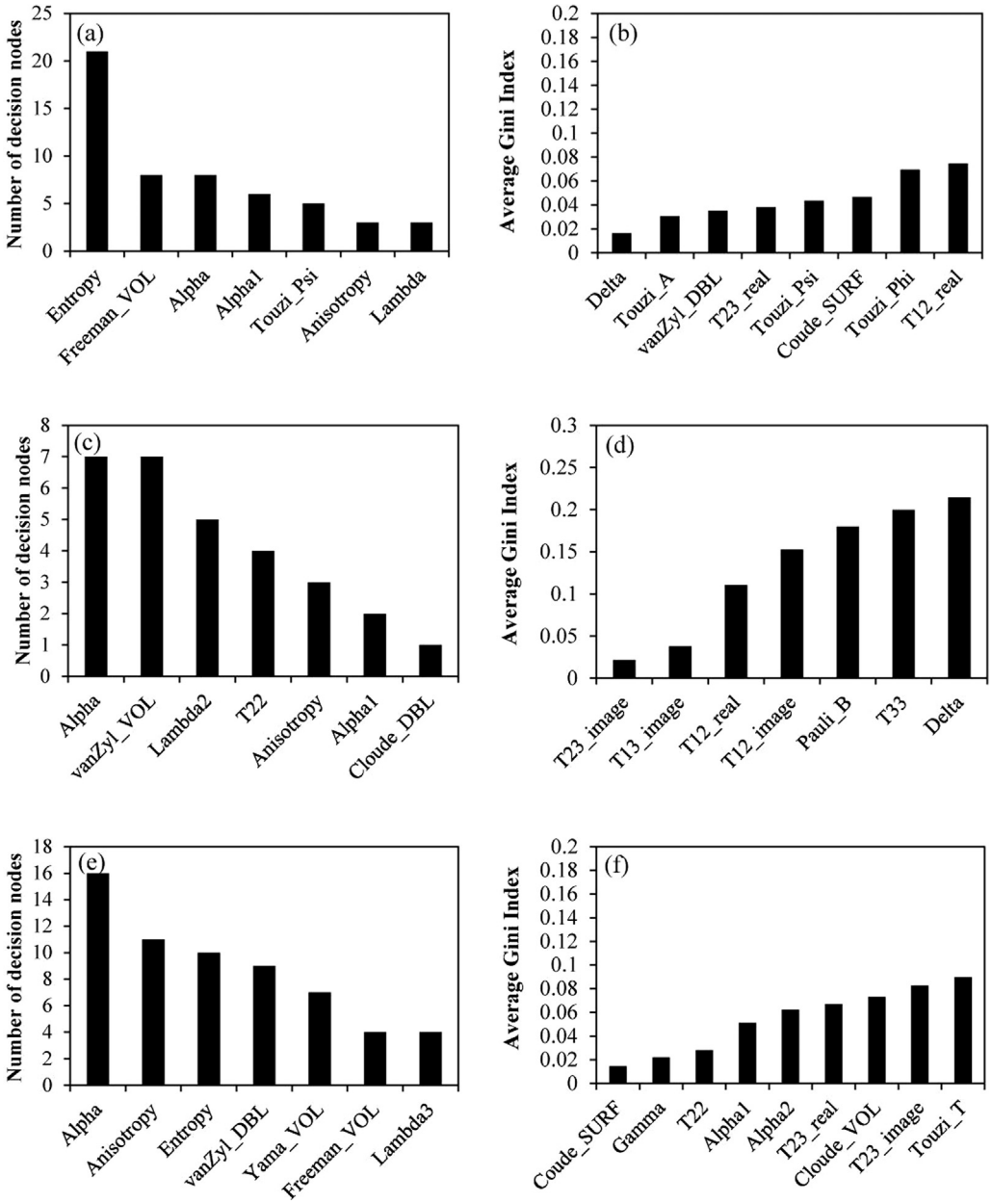

Fig. 9. The number of decision nodes and average Gini index for each feature in the CART.

4.4. Difficulty and land cover confusion assessment of the new scheme for ISC

Confusions between different land cover types have been widely identified in optical remote sensing data due to the confusion of spectral signatures between different land covers. This spectral confusion issue has been intensively studied and discussed as an important challenge in land use/land cover monitoring using optical remote sensing data. Similarly, under the new scheme of urban land cover classification using polarimetric SAR data, confusions between various land covers are also a challenging issue. However, these confusions are different than spectral confusions because of the special working mechanism of SAR remote sensing. In this section, two different measures were employed to assess these land cover confusions: (1) the number of result nodes (leaves) in the CART model, and (2) the producer's and user's accuracies, which were calculated from the confusion matrix based on the testing samples. Moreover, to provide a comprehensive understanding of the confusion issue, this assessment was conducted at three different levels, the subtypes of land covers level (Level III), the general land covers level (Level II) and the impervious surfaces and non-impervious surfaces level (Level I), which were presented in Table 4 of Section 3.2.

Fig. 10(a)–(c) illustrates the assessment at Level III classification of the three study sites. The observed patterns are quite different in the three cases. The numbers of leaves in CART were generally higher in Shenzhen and Macau than in Hong Kong, which may indicate that it was more difficult to classify the land covers in Shenzhen and Macau using CART. In the Shenzhen site, IS1, VEG1 and SOI had more result nodes than other land cover types, which showed the complexity of these classes. The complex classes were IS2, VEG1, VEG3 and SOI in Hong Kong, and VEG1, VEG2 and VEG3 in Macau. Therefore, we found that vegetation is a general challenge in all three cases, while other challenging classes were

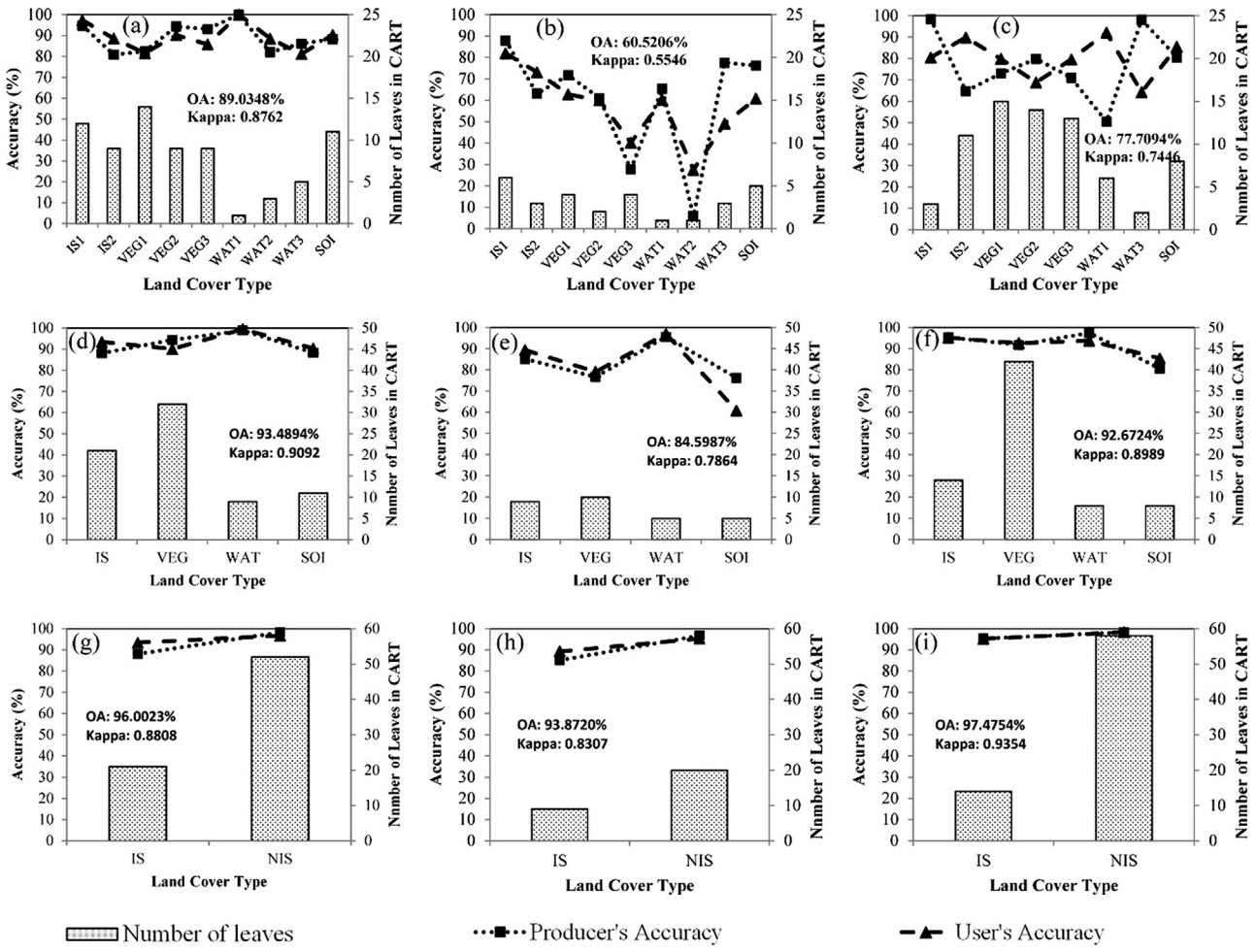

Fig. 10. Difficulty analysis at the level of land cover subclasses (a–c), general land covers (d–f) and impervious surfaces classification (g–i), panels a, d & g for Shenzhen, b, e & h for Hong Kong, c, f & i for Macau.

differed by case. The accuracy based on the confusion matrix also demonstrated different patterns in the three cases. The overall accuracy (OA) and Kappa coefficient were the highest in Shenzhen (OA: 89.03%; Kappa: 0.8762), while Hong Kong obtained the lowest accuracy (OA: 60.52%; Kappa: 0.5546). The producer's and user's accuracies showed that various land cover classes were well balanced in Shenzhen. In Hong Kong, the producer's and user's accuracies of VEG3 and WAT2 were rather low, which led to the low overall accuracy and Kappa coefficient. In contrast, the producer's and user's accuracies in Macau showed a fluctuation among different land cover classes but generally at a medium level. The OA in Macau was 77.71%, and the Kappa coefficient was 0.7446.

Confusions between various land cover subclasses are shown in Fig. 10(a)–(c), especially within the subclasses of impervious surfaces, vegetation and water surfaces. However, these subclasses were derived from their backscattering mechanism with polarimetric SAR data, and they do not have significant physical meaning in the real world. Therefore, these subclasses were combined to generate general land cover classes that had the same meaning as those generated from optical remote sensing, which are generally used in the urban planning and management fields. Fig. 10 (d)–(f) illustrates the results after combining the general land cover classes. Generally, the distribution of the number of result nodes in CART models was clearer among the land cover classes, and the overall accuracy and Kappa coefficient were improved over all the three cases. In all the three study sites, vegetation required the highest number of result nodes in the CART models, while water used the least nodes. The overall accuracy and Kappa coefficient were 93.49% and 0.9092 in Shenzhen, 84.60% and 0.7864 in Hong Kong and 92.67% and 0.8989 in Macau. These accuracies were comparable with those from land cover classifications using optical remote sensing data in previous studies (Zhang et al., 2012; Zhang et al., 2014). This result also indicated the effectiveness of urban land cover classification using polarimetric SAR data alone, without the additional support of optical data. However, we also observed several special difficulties of identifying certain land covers using polarimetric SAR data under the new scheme. For instance, the producer's and user's accuracies of vegetation and bare soil were generally lower than other land cover types, which was caused by the complex backscattering mechanisms illustrated in Fig. 4. With the highest producer's and user's accuracies, water surface was the easiest to recognize with the polarmetric SAR data.

Finally, the land cover classes of non-impervious surfaces were combined to generate the final impervious surfaces classification, and the number of result nodes in CARTs and the confusion-matrix-based accuracies were calculated (Fig. 10(g)–(i)), where two findings can be observed. First, the total number of result nodes for non-impervious surfaces was obviously higher than that of impervious surfaces. This is understandable because the non-impervious surfaces were much more complex and included various types of land covers and their subclasses. Additionally, the overall accuracy and Kappa coefficient were significant improved

and higher than 93% and 0.83, respectively, in all three cases. This result indicates the rather promising effectiveness of the newly proposed classification scheme for impervious surfaces classification. Moreover, the producer's and user's accuracies showed that non-impervious surfaces could be better recognized than impervious surfaces in the general condition. Interestingly, the overall accuracy and Kappa coefficient were highest in Shenzhen at the level of land cover types (Level II) and subtypes (Level III). Nevertheless, the highest accuracy in the final impervious surfaces classification was obtained in Macau. This result demonstrates that more of the land cover confusions happened among the non-impervious surfaces covers in Macau, and these confusions were avoided in the final impervious surfaces classification.

4.5. Comparison with ISC results using traditional scheme

In order to further assess the effectiveness of the proposed new scheme under the polarimetric SAR data, the traditional VIS-based scheme was employed to be compared. Since the VIS scheme only contains three components, vegetation, impervious surfaces and bare soils, the water component was added. Theoretically, the main differences between the traditional and the proposed schemes originate from the differences between the optical remote sensing data and SAR data that the former uses reflectance spectra features to distinguish impervious surface from other land cover types, while the latter uses backscattering features. In the traditional scheme, bright impervious surface is easily confused with dry bare soil due to their high spectral reflectance, while dark impervious surface is easily confused with water and shaded areas due to their low spectral reflectance (Weng, 2012; Weng and Hu, 2008; Wu et al., 2008; Zhang et al., 2015; Zhang et al., 2014). In the new scheme, these land cover confusions have been changed in SAR images because of their different backscattering features. Under the new scheme, impervious surface types located in Zones 1, 5, 7 and 8 are less confused with other land covers since their backscattering mechanisms are typical, shown in Fig. 4. However, instead, confusions occur between impervious surface types and non-impervious surface types in Zones 2&4, where IS2 is confused with VEG1 and IS1 is confused with VEG3 and WAT2. These backscattering confusions remain difficult to address in the proposed scheme. One possible solution is to incorporate optical and SAR images, since these confusions may be not confused in optical images. Therefore, one recommendation about the future work is to incorporate optical and SAR images to reduce the confusions shown in Zones 2 and 4.

In order to provide a more reasonable comparison, all the polarimetric features were the same in both traditional approach and this study. Then, the implementation of the traditional approach for impervious surfaces classification was a two-step approach, land cover classification at Level II and combinations of impervious classes at Level I (Table 4). Therefore, the comparison between the traditional approach and the proposed approach can only be conducted at Level II and Level I. Moreover, the same samples were used as the testing samples for accuracy assessment. The confusion matrix and accuracy assessment were shown in Table 6 (Level II) and Table 7 (Level I). Firstly, Table 6 demonstrated the classification at Level II, where both the overall accuracy and Kappa coefficients were generally improved by about 1–4% over the three study cases. Shenzhen and Hong Kong witnessed more improvement with a significant reduce of confusion between impervious surfaces and vegetation. This was consistent with the previous findings in this study that different subclasses of vegetation can have confusions with different subclasses of impervious surfaces, in Zones 2&4 in Fig. 4. The results indicated that the use of subclasses in Level III was able to improve the classification results as it considered the scattering mechanisms of each subclass of the traditional VIS-based classes. However, the classification of water surface and bare soil did not have significant difference between the traditional and proposed approaches.

Secondly, after combining the impervious classes and non-impervious classes, Table 7 demonstrates the accuracy assessment results of the comparison at Level I. The overall accuracy and Kappa coefficients increased in the classification at Level I. However, when comparing the accuracies between the traditional and pro-

Table 6
Confusion matrix (Level II) between the proposed and traditional schemes.

	IS	VEG	WAT	SOI	This Study	IS	VEG	WAT	SOI	Traditional
IS	338	21	0	3	Shenzhen:	263	0	0	9	Shenzhen:
VEG	42	597	2	22	OA: 93.49%; Kappa: 0.9092	107	601	1	23	OA: 89.03%; Kappa: 0.8462
WAT	0	2	506	1		0	2	505	0	
SOI	4	13	4	196		14	30	6	190	
IS	381	45	0	1	Hong Kong:	249	1	0	0	Hong Kong:
VEG	64	479	21	42	OA: 84.60%; Kappa: 0.7864	198	592	35	85	OA: 80.69%; Kappa: 0.7238
WAT	0	16	556	2		0	0	543	0	
SOI	3	85	5	144		1	32	4	104	
IS	412	14	0	7	Macau:	361	13	0	2	Macau:
VEG	20	521	7	15	OA: 92.67%; Kappa: 0.8989	59	529	0	14	OA: 91.57%; Kappa: 0.8827
WAT	0	8	402	19		0	2	596	19	
SOI	0	25	4	170		5	24	15	176	

Table 7
Confusion matrix (Level I) between the proposed and traditional schemes.

	IS	NIS	This Study	IS	VEG	Traditional
IS	338	24	Shenzhen:	263	9	Shenzhen:
NIS	46	1343	OA: 96.00%; Kappa: 0.8808	121	1358	OA: 92.58%; Kappa: 0.7578
IS	381	46	Hong Kong:	249	1	Hong Kong:
NIS	67	1350	OA: 93.87%; Kappa: 0.8307	199	1395	OA: 89.15%; Kappa: 0.6531
IS	412	21	Macau:	361	15	Macau:
NIS	20	1171	OA: 97.46%; Kappa: 0.9354	64	1375	OA: 95.65%; Kappa: 0.8736

posed schemes, both the overall accuracy and Kappa coefficient increased by 1.5–4.6%, which was higher than that at Level II. This result indicated that the confusion between vegetation and impervious surfaces was playing a key role during the classification using polarimetric SAR data, and hence the reducing of this confusion was able to improve the accuracy on the final impervious surfaces classification.

5. Conclusions

The backscattering mechanism of polarimetric SAR data for urban land cover classification and impervious surfaces classification was investigated in this study. Compared with the V-I-S conceptual model for mapping impervious surfaces in optical remote sensing data, this paper proposed a new classification scheme by defining different land cover subtypes according to their polarimetric backscattering mechanism. Three scenes of fully polarimetric Radsarsat-2 data in the cities of Shenzhen, Hong Kong and Macau were employed to test and validate the proposed methodology. Several interesting findings were observed. First, the importance of different polarimetric features and land cover confusions were investigated and indicated that the alpha, entropy and anisotropy from the H/A/Alpha decomposition were more important than other features. One or two, but not all, components from other decompositions also contributed to the results. Additionally, the confusion and difficulty analyses demonstrated that vegetation was a challenging and difficult land cover to identify in SAR data because it was confused with impervious surfaces in different ways, including double bounce scattering, volume scattering and surface scattering. Finally, the accuracy assessment showed that the overall accuracy and Kappa coefficient were 96.00% and 0.8808 in Shenzhen, 93.87% and 0.8307 in Hong Kong and 97.48% and 0.9354 in Macau, respectively, indicating the promising applicability and great potential of the new scheme for impervious surfaces classification using polarimetric SAR data.

Acknowledgments

This study was jointly supported by National Natural Science Foundation of China (41401370) and the Research Grants Council (RGC) General Research Fund (CUHK 14601515, CUHK 14635916 and CUHK 14605917), and the support of Zhuhai Joint Innovative Center for Climate-Environment-Ecosystem, Future Earth Research Institute, Beijing Normal University, Zhuhai 519087, China. The authors would like to thank the anonymous reviewers and editor for their critical comments and suggestions to improve the original manuscript.

References

Arnold, C.L., Boison, P.J., Patton, P.C., 1982. Sawmill brook – an example of rapid geomorphic change related to urbanization. J. Geol. 90, 155–166.
Arnold, C.L., Gibbons, C.J., 1996. Impervious surface coverage – The emergence of a key environmental indicator. J. Am. Plann. Assoc. 62, 243–258.
Bannerman, R.T., Owens, D.W., Dodds, R.B., Hornewer, N.J., 1993. Sources of pollutants in wisconsin stormwater. Water Sci. Technol. 28, 241–259.
Bhattacharya, A., Touzi, R., 2011. Polarimetric SAR urban classification using the Touzi target scattering decomposition. Can. J. Remote Sens. 37, 323–332.
Calabresi, G., 1996. The Use of ERS Data for Flood Monitoring: An Overall Assessment, Second ERS Application Workshop. European Space Agency, London, UK, Noordwijk, Netherlands, pp. 237–241.
Cloude, S.R., Pottier, E., 1997. An entropy based classification scheme for land applications of polarimetric SAR. IEEE T. Geosci. Remote 35, 68–78.
Dekker, R.J., 2003. Texture analysis and classification of ERS SAR images for map updating of urban areas in the Netherlands. IEEE T. Geosci. Remote 41, 1950–1958.
Deng, C.B., Wu, C.S., 2013. Examining the impacts of urban biophysical compositions on surface urban heat island: A spectral unmixing and thermal mixing approach. Remote Sens. Environ. 131, 262–274.
Dong, Y., Forster, B., Ticehurst, C., 1997. Radar backscatter analysis for urban environments. Int. J. Remote Sens. 18, 1351–1364.
Espey, W.H., Morgan, C.W., Masch, F.D., 1966. Study of Some Effects of Urbanization on Storm Runoff from a Small Watershed. Texas Water Development Board, Report 23.
Gamba, P., Aldrighi, M., 2012. SAR data classification of urban areas by means of segmentation techniques and ancillary optical data. IEEE J.-Stars. 5, 1140–1148.
Gamba, P., Lisini, G., 2013. Fast and efficient urban extent extraction using ASAR wide swath mode data. IEEE J.-Stars. 6, 2184–2195.
Guo, H.D., Yang, H.N., Sun, Z.C., Li, X.W., Wang, C.Z., 2014. Synergistic use of optical and PolSAR imagery for urban impervious surface estimation. Photogramm. Eng. Rem. S. 80, 91–102.
Hariharan, S., Tirodkar, S., Bhattacharya, A., 2016. Polarimetric SAR decomposition parameter subset selection and their optimal dynamic range evaluation for urban area classification using Random Forest. Int. J. Appl. Earth Obs. 44, 144–158.
Henderson, F.M., Xia, Z.G., 1997. SAR applications in human settlement detection, population estimation and urban land use pattern analysis: A status report. IEEE T. Geosci. Remote 35, 79–85.
Hu, H.T., Ban, Y.F., 2012. Multitemporal RADARSAT-2 ultra-fine beam SAR data for urban land cover classification. Can. J. Remote Sens. 38, 1–11.
Hu, X.F., Waller, L.A., Lyapustin, A., Wang, Y.J., Al-Hamdan, M.Z., Crosson, W.L., Estes, M.G., Estes, S.M., Quattrochi, D.A., Puttaswamy, S.J., Liu, Y., 2014. Estimating ground-level PM2.5 concentrations in the Southeastern United States using MAIAC AOD retrievals and a two-stage model. Remote Sens. Environ. 140, 220–232.
Hu, X.F., Weng, Q.H., 2009. Estimating impervious surfaces from medium spatial resolution imagery using the self-organizing map and multi-layer perceptron neural networks. Remote Sens. Environ. 113, 2089–2102.
Hu, X.F., Weng, Q.H., 2011. Estimating impervious surfaces from medium spatial resolution imagery: a comparison between fuzzy classification and LSMA. Int. J. Remote Sens. 32, 5645–5663.
Jacobson, C.R., 2011. Identification and quantification of the hydrological impacts of imperviousness in urban catchments: A review. J. Environ. Manage. 92, 1438–1448.
Jensen, J.R., 2007. Introductory Digital Image Processing: A Remote Sensing Perspective. Pearson Education Ltd., London.
Kim, H., Loh, W.Y., 2001. Classification trees with unbiased multiway splits. J. Am. Stat. Assoc. 96, 589–604.
Lee, J.-S., Pottier, E., 2009. Polarimetric Radar Imaging: From Basics to Applications. CRC Press.
Li, X.W., Pottier, E., Guo, H.D., Ferro-Famil, L., 2010. Urban land cover classification with high-resolution polarimetric SAR interferometric data. Can. J. Remote Sens. 36, 236–247.
Loh, W.Y., 2011. Classification and regression trees. Wires Data Min. Knowl. 1, 14–23.
Lu, D.S., Weng, Q.H., 2006. Use of impervious surface in urban land-use classification. Remote Sens. Environ. 102, 146–160.
Majd, M.S., Simonetto, E., Polidori, L., 2012. Maximum likelihood classification of single high-resolution polarimetric SAR images in urban areas. Photogramm. Fernerkun., 395–407
Niu, X., Ban, Y.F., 2013. Multi-temporal RADARSAT-2 polarimetric SAR data for urban land-cover classification using an object-based support vector machine and a rule-based approach. Int. J. Remote Sens. 34, 1–26.
Niu, X., Ban, Y.F., 2014. A novel contextual classification algorithm for multitemporal polarimetric SAR data. IEEE Geosci. Remote S. 11, 681–685.
Ooi, M.C.G., Chan, A., Ashfold, M.J., Morris, K.I., Oozeer, M.Y., Salleh, S.A., 2017. Numerical study on effect of urban heating on local climate during calm inter-monsoon period in greater Kuala Lumpur, Malaysia. Urban Clim. 20, 228–250.
Park, S.E., Moon, W.M., 2007. Unsupervised classification of scattering mechanisms in polarimetric SAR data using fuzzy logic in entropy and alpha plane. IEEE T. Geosci. Remote 45, 2652–2664.
Pellizzeri, T.M., 2003. Classification of polarimetric SAR images of suburban areas using joint annealed segmentation and "H/A/alpha" polarimetric decomposition. Isprs J. Photogramm. 58, 55–70.
Ridd, M.K., 1995. Exploring a V-I-S (Vegetation-Impervious Surface-soil) model for urban ecosystem analysis through remote-sensing – comparative anatomy for cities. Int. J. Remote Sens. 16, 2165–2185.
Schueler, T., 1994. The importance of imperviousness. Watershed Protect. Techn. 1, 100–111.
Seabum, G.E., 1969. Effects of urban development on direct runoff to East Meadow Brook, Nassau County, Long Island, New York, Professional Paper 627-B., U.S. Geological Survey, Washington, D.C.
Sleavin, W.J., Civco, D.L., Prisloe, S., Giannotti, L., 2000. Measuring impervious surfaces for non-point source pollution modeling, Proceedings of 2000 ASPRS Annual Convention, Washington, D.C.
Slonecker, E.T., Jennings, D.B., Garofalo, D., 2001. Remote sensing of impervious surfaces: A review. Remote Sens. Rev. 20, 227–255.
Stasolla, M., Gamba, P., 2008. Spatial indexes for the extraction of formal and informal human settlements from high-resolution SAR images. IEEE J.-Stars. 1, 98–106.
Tison, C., Nicolas, J.M., Tupin, F., Maitre, H., 2004. A new statistical model for Markovian classification of urban areas in high-resolution SAR images. IEEE T. Geosci. Remote 42, 2046–2057.
Van de Voorde, T., Jacquet, W., Canters, F., 2011. Mapping form and function in urban areas: An approach based on urban metrics and continuous impervious surface data. Landscape Urban Plan. 102, 143–155.

Voisin, A., Krylov, V.A., Moser, G., Serpico, S.B., Zerubia, J., 2013. Classification of very high resolution SAR images of urban areas using copulas and texture in a hierarchical markov random field model. IEEE Geosci. Remote S. 10, 96–100.
Weng, Q.H., 2001. Modeling urban growth effects on surface runoff with the integration of remote sensing and GIS. Environ. Manage. 28, 737–748.
Weng, Q.H., 2012. Remote sensing of impervious surfaces in the urban areas: Requirements, methods, and trends. Remote Sens. Environ. 117, 34–49.
Weng, Q.H., Hu, X.F., 2008. Medium spatial resolution satellite imagery for estimating and mapping urban impervious surfaces using LSMA and ANN. IEEE T. Geosci. Remote 46, 2397–2406.
Weng, Q.H., Lu, D.S., Liang, B.Q., 2006. Urban surface biophysical descriptors and land surface temperature variations. Photogramm. Eng. Rem. S. 72, 1275–1286.
Wu, C.S., Murray, A.T., 2003. Estimating impervious surface distribution by spectral mixture analysis. Remote Sens. Environ. 84, 493–505.
Wu, Y.H., Ji, K.F., Yu, W.X., Su, Y., 2008. Region-based classification of polarimetric SAR images using wishart MRF. IEEE Geosci. Remote S. 5, 668–672.
Yang, F., Matsushita, B., Fukushima, T., 2010. A pre-screened and normalized multiple endmember spectral mixture analysis for mapping impervious surface area in Lake Kasumigaura Basin, Japan. Isprs J. Photogramm. 65, 479–490.
Yuan, F., Bauer, M.E., 2007. Comparison of impervious surface area and normalized difference vegetation index as indicators of surface urban heat island effects in Landsat imagery. Remote Sens. Environ. 106, 375–386.
Zhang, H., Li, J., Wang, T., Lin, H., Zheng, Z., Li, Y., Lu, Y., 2018. A manifold learning approach to urban land cover classification with optical and radar data. Landscape Urban Plan. 172, 11–24.
Zhang, H., Zhang, Y., Lin, H., 2012. A comparison study of impervious surfaces estimation using optical and SAR remote sensing images. Int. J. Appl. Earth Obs. 18, 148–156.
Zhang, H.S., Lin, H., Li, Y., Zhang, Y.Z., 2013. Feature extraction for high-resolution imagery based on human visual perception. Int. J. Remote Sens. 34, 1146–1163.
Zhang, H.S., Lin, H., Li, Y., Zhang, Y.Z., Fang, C.Y., 2016. Mapping urban impervious surface with dual-polarimetric SAR data: An improved method. Landscape Urban Plan. 151, 55–63.
Zhang, H.S., Lin, H., Zhang, Y.Z., Weng, Q.H., 2015. Remote Sensing of Impervious Surfaces in Tropical and Subtropical Areas. CRC Press.
Zhang, H.S., Xu, R., 2018. Exploring the optimal integration levels between SAR and optical data for better urban land cover mapping in the Pearl River Delta. Int. J. Appl. Earth Obs. 64, 87–95.
Zhang, L.M., Zou, B., Zhang, J.P., Zhang, Y., 2010. Classification of polarimetric SAR image based on support vector machine using multiple-component scattering model and texture features. Eurasip J. Adv. Sig. Pr.
Zhang, Y.Z., Zhang, H.S., Lin, H., 2014. Improving the impervious surface estimation with combined use of optical and SAR remote sensing images. Remote Sens. Environ. 141, 155–167.